Electronic and thermal signatures of phosphorene grain boundaries under uniaxial strain

Álvaro Rodríguez Méndez [1,2] Leonardo Medrano Sandonas [3] Arezoo Dianat [1]
Rafael Gutierrez [1,*] and Gianaurelio Cuniberti [1,4]

[1]*Institute for Materials Science and Max Bergmann Center of Biomaterials, TU Dresden, 01062 Dresden, Germany*
[2]*Max Planck Institute for the Physics of Complex Systems, 01187 Dresden, Germany*
[3]*Department of Physics and Materials Science, University of Luxembourg, L-1511 Luxembourg, Luxembourg*
[4]*Dresden Center for Computational Materials Science (DCMS), TU Dresden, 01062 Dresden, Germany*

(Received 29 July 2022; accepted 27 October 2022; published 17 November 2022)

Two-dimensional materials have great potential for applications as high-performance electronic devices and efficient thermal rectificators. Among them, pristine phosphorene, a single layer of black phosphorus, has shown promising properties such as ultrahigh charge mobility, a tunable band gap, and mechanical flexibility. However, the introduction of extended structural defects such as grain boundaries (GBs) has, in general, a detrimental influence on the electronic and thermal transport properties by causing additional scattering events. In this computational study, based on a combination of a density-functional parametrized tight-binding approach with the Landauer theory of quantum transport, we show that applying a strain can help to partially counteract this effect. We exemplify this by addressing the electronic and phononic transmission of two specific grain boundaries containing 5|7 (GB1) and 4|8 (GB2) defects, respectively. Under uniaxial strain, the electronic band gaps can be reduced for both types of GB, while the respective thermal conductance is only weakly affected despite rather strong changes in the frequency-resolved phonon transmission. The combination of both effects mainly produces an increase of about a factor of 2 in the thermoelectric figure of merit ZT for a GB2 system. Hence, our results provide insights into the manipulation of transport properties as well as the generation of potential thermoelectric materials based on phosphorene.

DOI: 10.1103/PhysRevMaterials.6.114003

I. INTRODUCTION

Since the fabrication of graphene by mechanical exfoliation [1], there has been an increasingly accelerated search for novel two-dimensional (2D) materials, a search largely motivated by their remarkable physical and chemical properties related to strong quantum confinement effects originating in the reduced spatial dimensionality; see, e.g., Refs. [2–6].

Phosphorene, the 2D version of black phosphorus, represents a promising candidate for electronic and optoelectronic applications because of its distinctive properties, such as ultrahigh charge mobility, a tunable direct band gap, mechanical flexibility, and anisotropic structure [7,8]. This material was successfully exfoliated from bulk black phosphorus into a mono- or few-layered material [9]. Its geometry resembles the graphene structure from a top perspective, but it consists of a nonplanar puckered honeycomb lattice, where each P atom is bonding with three neighboring P atoms with an sp^3 hybridization. Unlike the zero-band-gap graphene, bulk layered phosphorus has a direct band gap at the Γ point of 0.3 eV, which increases in mono- or few-layer phosphorene up to 2.0 eV [10,11]. Strategies to tune the electronic, thermal, and optical properties of black phosphorene have been studied, including doping [12], varying the number of layers [13], applying mechanical stress [14], or through the formation of grain boundaries in polycrystalline materials [15]. Concerning the polycrystallinity issue, it is well known that most bulk or 2D materials, either synthesized or extracted from nature, are not comprised of single-crystal units, but rather of multiple crystals in a network of multiple interfaces. The resulting grain boundaries (GBs) can significantly affect the properties of the material when compared with the bulk counterpart [16–18]. For instance, the misorientation angle was found to be a parameter influencing the average electrical conductivity of graphene GBs, where a minimum of conductivity can be reached when the GB misorientation angle reaches 30° [19]. A multiscale modeling study of silicene showed that the Kapitza thermal conductance varies according to the GB type and size, finding that its thermal conductivity can be modulated up to one order of magnitude [20]. Another example involves borophene GBs, where the introduction of a GB modifies the electronic states around the Fermi level due to backscattering, but without destroying its metallic character [21]. Regarding phosphorene GB, a density functional theory (DFT) study of 19 different GBs showed that the GB formation energies were smaller than the required formation energies of other 2D GBs such as in graphene and molybdenum disulfide [22]. Moreover, the authors stated that no major variations in the low-energy electronic properties of phosphorene were expected, since no midgap states were introduced by the GB formation, so that the systems remained direct-band-gap semiconductors. Further studies have also shown that the misorientation angle and the GB direction (zigzag or

*rafael.gutierrez@tu-dresden.de

armchair) modify their energetic [22–24] and mechanical stability [15,25] as well as the electronic and thermal properties [22,26,27].

Mechanical strain in 2D materials has been used quite often to modify the electronic band structure for engineering materials with tuned electronic performance; see, e.g., the recent reviews in Refs. [28,29]. Similarly, strain engineering can be exploited to influence the thermal properties [30]; for instance, a DFT study of 2D hexagonal boron arsenide showed that thermal conductivity can be enhanced by a factor of 2 upon applying strain [31]. Also, an experimental study of multilayer graphene has shown that the thermal conductivity is highly sensitive towards strain, finding a decrease of ∼70% after applying only a 0.1% strain [32]. Other theoretical studies have found a similar behavior for molybdenum disulfide and hexagonal boron nitride, where the thermal conductance continuously decreased upon increasing the strain level [33]. In the present computational investigation, we address the influence of two specific grain boundary types (containing 5|7 and 4|8 defects) on the electronic and thermal transport properties of phosphorene, while additionally applying a uniaxial strain. For this, we combine a density functional tight-binding based approach with an atomistic Green's function formalism to compute the corresponding quantum transport properties at the level of the Landauer theory. Our results show that the GB increases the electronic band gap for both systems, and that the applied strain can be used to modulate the band gap, reaching half of the value of pristine phosphorene. On the other hand, the presence of the GB decreases the phonon transmission in the systems, but further modulation of it by the applied strain depends on the GB type. Finally, we found that the thermoelectric figure of merit of pristine phosphorene is enhanced by considering both GB types, reaching almost twice its value for GB2. This thermoelectric performance is subsequently tuned by the applied strain and temperature.

II. METHODS

A. Model systems

Here, two specific grain boundaries were considered for investigating their effect on the electronic and thermal properties of phosphorene. The first system, denoted by GB1, consists of two zigzag phosphorene monolayers with a misorientation angle of 26.8° forming a GB containing 5|7 defects. The second system, named GB2, consists of two armchair phosphorene monolayers with a misorientation angle of 31.8° forming a GB containing 4|8 defects [see Figs. 1(a) and 1(b)]. These types of GB are the most reported in experimental studies of other 2D materials [34–36] as well as in computational works of phosphorene GB [15,23].

The geometry optimization, electronic Hamiltonian matrix, and interatomic force constant calculations were carried out by using a density functional tight-binding (DFTB) method as implemented in the DFTB+ code [37]. The DFTB method has been successfully used for the simulation of the electronic and thermal properties of diverse low-dimensional materials [38–40]. The Slater-Koster parameter set Mio-1-1 [41] is used for our calculations, and geometry optimization is performed using the conjugate gradient method with a convergence threshold in forces of 10^{-5} a.u. and considering periodic boundary conditions along the y-axis (GB direction).

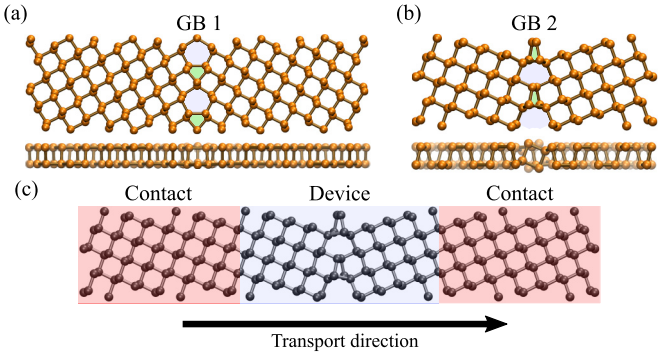

FIG. 1. Atomistic representation from top and side views of the two phosphorene grain boundaries studied in this work: (a) GB1 system (5|7 defect) and (b) GB2 system (4|8 defect). Both systems were built up with two zigzag and armchair phosphorene monolayers, respectively. The blue and green shades highlight the regions of the grain boundaries in the middle of the system. (c) Representation of the common partitioning scheme for electronic and phononic transmission calculations as described in the text. The contact region contains 128 atoms for GB1 and 50 atoms for GB2.

B. Electron and phonon transport

The atomistic Green's function formalism was used to compute the electronic and thermal transport properties [42]. To do so, our systems are treated within the common partition scheme, which splits a system into three regions: two contacts (left and right) and a device or scattering region [see Fig. 1(c)] [43]. Each contact for GB1 and GB2 consisted of 128 atoms and 50 atoms, respectively, whereas, the device region included 172 atoms for GB1 and 92 atoms GB2. We introduced strain in both systems along the transport direction. The rows of atoms of the device that are near the contacts have the same unit cell as the contacts themselves, therefore we will have scattering around the GB only. This situation will hold for systems with and without applied strain. The geometry optimization of the GB systems with applied strain was carried in a two-step calculation. We first stretched the atoms in the two extremes of the device region along the transport axis and optimized the geometry. Then, we fixed the coordinates of the atoms in the transport axis and optimized the unit-cell parameter in the axis perpendicular to the transport one to avoid additional stress. The strain level was calculated as $s = (L - L_0)/L_0$, where L_0 is the length of the whole system (device and contact regions) along the transport direction, and L corresponds to the length of the whole system after applying strain. The calculations were performed with periodic boundary conditions in the direction perpendicular to the transport axis.

The transport calculations were carried out in the frame of the Landauer approach. The electronic and phonon channels were treated independently, and the quantities of interest to be computed were the electronic and phononic transmission functions [$\tau_{el}(E)$ and $\tau_{ph}(\omega)$, respectively]. The electronic transmission coefficient is calculated by the following

equation:

$$\tau_{\rm el}(E) = {\rm Tr}(G^r \Gamma_L G^a \Gamma_R), \tag{1}$$

where G^r is the retarded Green's function of the central region computed as $G^r = (EI - H - \Sigma_L^r - \Sigma_R^r)^{-1}$, the Hamiltonian matrix is represented by H, E is the energy of the electrons, and I is the unit matrix. The broadening function $\Gamma_{L/R} = i[\Sigma^r_{L/R} - \Sigma^a_{L/R}]$ defines the reservoir spectral densities, from where the retarded/advanced self-energies $\Sigma^{r/a}_{L/R}$ encode the electronic structure of both the semi-infinite reservoirs and the reservoir-central region interface.

The phononic transmission $\tau_{\rm ph}(\omega)$ is computed with a similar mathematical procedure to $\tau_{\rm el}(E)$, but replacing $H \to K$ and $EI \to \omega^2 I$, where K is the dynamical matrix [43]. The thermal conductance is then obtained as follows:

$$\kappa_{\rm ph} = \frac{1}{2\pi}\int_0^\infty d\omega\,(\hbar\omega)\frac{dN_B}{dT}\tau_{\rm ph}(\omega), \tag{2}$$

where k_B and N_B are the Boltzmann constant and the Bose-Einstein distribution, respectively. The transport calculations were performed by using the libNEGF [44] and PHONON [45] modules implemented in the DFTB+ code.

III. RESULTS

A. Structural properties

We first analyzed the stability of phosphorene GB1 and GB2. In doing so, we have calculated the formation energy per atom ($E_{\rm form}$) of both GB systems according to $E_{\rm form} = (\epsilon_{\rm GB} - N \times \epsilon_P)/2L_0$ [23]. $\epsilon_{\rm GB}$ is the energy of the GB system comprised by the number N of phosphorous atoms, ϵ_P is the energy per atom of pristine phosphorene, and L_0 is the length of the whole system. We found that $E_{\rm form} = 1.02$ eV/nm for GB1 is lower than the corresponding one for GB2 ($E_{\rm form} = 1.56$ eV/nm), i.e., GB1 is energetically more favorable and stable than GB2. The reason behind the low-energy formation can be attributed to the sp^3 hybridization of P atoms, which allows more dislocations than other systems with sp^2 hybridization like graphene. Even though GB2 shows a relatively high $E_{\rm form}$ value, it is still within the energy range 0.9–2.43 eV/nm, which was reported in the extensive study about the energetic stability of phosphorene GB done by Guo *et al.* [22]. Moreover, this energy window is lower than the one corresponding to other GB materials like graphene and molybdenum disulfide, implying that these phosphorene GBs may be experimentally viable [22].

Then we proceed with the analysis of the systems after applying strain, where uniaxial strain along the transport direction (perpendicular to the GB) was applied in the complete system. In Fig. 2, we analyze the change in relative length $\Delta B_{\rm Fx} = [B_{\rm Fx}(s) - B_{\rm Fx}(s=0)]/B_{\rm Fx}(s=0)$ of some selected bonds Fx around the grain boundary as a function of the applied uniaxial strain s. Here, $B_{\rm Fx}(s)$ denotes the bond length of bond Fx under applied strain, and $B_{\rm Fx}(s=0)$ is the corresponding equilibrium bond length in the absence of any strains. The index x numbers the bonds shown in Fig. 2. A positive value of $\Delta B_{\rm Fx}$ means enlargement of the bond, while negative $\Delta B_{\rm Fx}$ denotes compression. Moreover, we defined two different types of bonds—in-plane (IP) and out-of-plane (OP)—and corresponding to them, average values $\Delta B_{\rm IP(OP)}$, which are computed in a similar way to $\Delta B_{\rm Fx}$, but using the average values of B and B_0. Regarding GB1 [see Figs. 2(a) and 2(b)], one can see that $\Delta B_{\rm IP}$ for IP bonds increases gradually with the applied strain (red filled circles), while it decreases for OP bonds (black filled circles). This reduction originates from the biatomic layer structure of phosphorene, which also contains voids allowing the displacement of phosphorous atoms when the material is uniaxially stretched. Moreover, the growth rate of the length of IP bonds is larger than the reduction rate of OP bonds, highlighting the stronger strain dependence of IP bonds. Comparing the individual IP bonds (F1, F2, F3), we see that $\Delta B_{\rm F2}$ and $\Delta B_{\rm F3}$ show a close behavior to the average $\Delta B_{\rm IP}$ value, which mostly corresponds to the regions next to the GB. In contrast, $\Delta B_{\rm F1}$ and $\Delta B_{\rm F2}$ are oriented along a similar direction, but $\Delta B_{\rm F1}$ has a higher growth rate compared to the average $\Delta B_{\rm IP}$. Moving to the OP bonds (F4 and F5), $\Delta B_{\rm F4}$ and $\Delta B_{\rm F5}$ displayed very similar strain dependence, $\Delta B_{\rm F4}$ showing a slighter larger reduction rate. Accordingly, the bonds between the atoms closer to the GB are more sensitive to the applied strain.

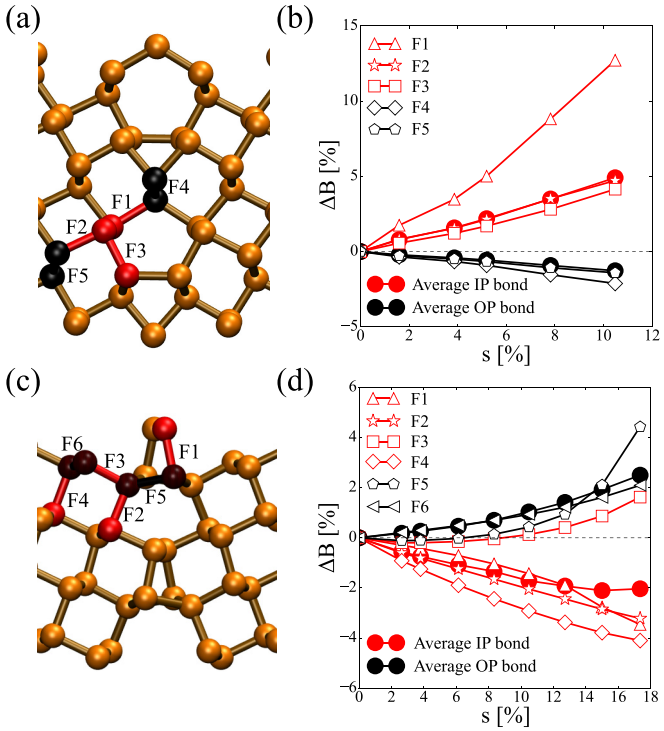

FIG. 2. Bond analysis of the device region in (a),(b) GB1 and (c),(d) GB2 systems with and without strain. Panels (a) and (c) show a top view of the grain boundaries, and highlighted in red and black are the in-plane (IP) and out-of-plane (OP) bonds, respectively, that were considered for further analysis. Panels (b) and (d) show the relative bond-length change (ΔB) upon applied strain. The different quantities plotted here are explained in the main text. The results in red correspond to the IP bonds, and those in black correspond to the OP bonds. The empty markers correspond to the bonds highlighted in panels (a) and (c), while the filled markers correspond to in-plane and out-of-plane bond-length changes, averaged over the whole device region.

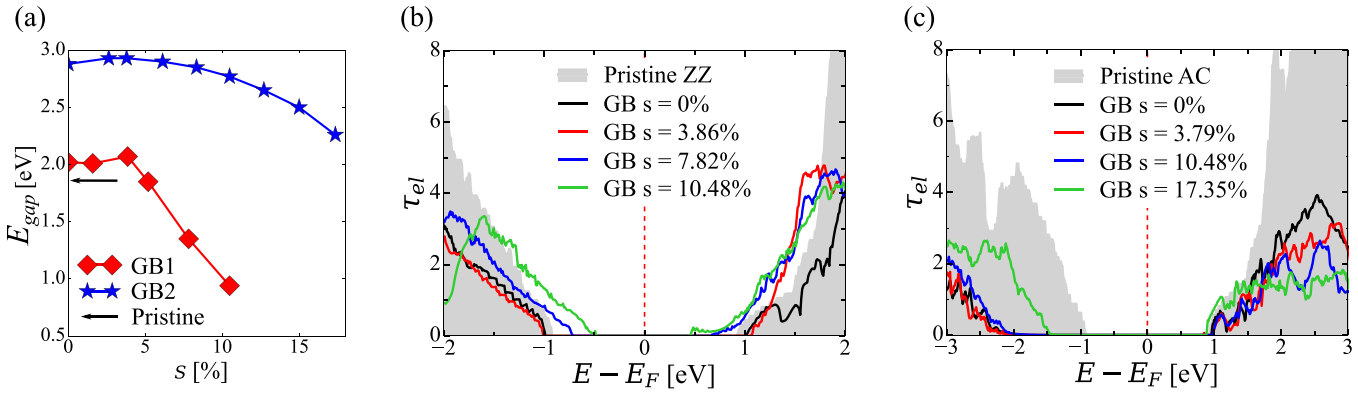

FIG. 3. (a) Electronic band gap E_{gap} of GB1 (red) and GB2 (blue) systems as a function of the applied strain. The horizontal arrow shows the position of E_{gap} of pristine phosphorene. Electronic transmission τ_{el} as a function of the energy for (b) GB1 and (c) GB2 systems without and with applied strain. As a reference, the corresponding transmission functions of pristine phosphorene in the zigzag (ZZ) and armchair (AC) directions were included in the graphics as a gray background.

On the other hand, the IP and OP bonds in GB2 [Figs. 2(c) and 2(d)] show a different behavior from the one found in GB1. The average ΔB_{IP} decreases with the applied strain, while the average ΔB_{OP} increases. This difference mostly relates to the difference between armchair and zigzag directions in phosphorene. Looking at the armchair system (GB2) from left to right in the direction where the strain was applied, one can see that the P atoms are connected by alternating IP and OP bonds, i.e., it is not possible to find a path that connects phosphorus atoms on the top layer from left to right without passing through an OP bond, whereas for the zigzag system (GB1) atoms are connected via IP bonds on the bottom and top layer. We also found that the atoms closer to the grain boundary in the system GB2 are positioned on different heights compared to the rest of the system, which might cause a different behavior in ΔB_{Fx} as a function of the applied strain. In particular, ΔB_{F1} and ΔB_{F5} show higher values after straining the system above $s = 13\%$. These effects will have an impact on the electronic couplings and force constants between the atoms in various regions of the systems, which will be reflected in their corresponding electronic and thermal transport properties, as shown later.

B. Electronic properties

Next, we analyzed the strain dependence of the electronic band gap E_{gap} of GB1 (red line) and GB2 (blue line) systems; see Fig. 3(a).

These systems initially display E_{gap} larger than the one corresponding to pristine phosphorene (black arrow), which exemplifies a way of modifying the pristine E_{gap} by appropriate introduction of structural defects. The influence of GB depends on the pristine material, e.g., GB in graphene may open an electronic gap [46], while the opposite behavior was reported for molybdenum disulfide [47]. In this work, the 5|7 defects slightly increase E_{gap} up to 2.0 eV, while the 4|8 defects produced a larger increment up to 2.9 eV (1.1 eV more than the pristine case). These results in E_{gap} are in agreement with a study performed on the thermodynamic stability of phosphorene GB and their electronic properties using density functional theory [22]. When uniaxial strain is applied, the E_{gap} of both GBs first slightly increases due to the compression of the (top and bottom) atomic layers; however, it then decreases for $s \geqslant 5\%$. In fact, the E_{gap} for the GB1 system reaches a value of 1.0 eV at $s \approx 10\%$, and for the GB2 system it goes down to 2.2 eV at $s = 18\%$, implying a decrease of 50% and 24% for GB1 and GB2 after applied strain, respectively. This strain-induced nonmonotonous change of E_{gap} has also been observed on other systems such as graphene nanoribbons [48] and a hybrid system composed of graphane and fluorographane [49]. This effect can be explained by considering the location of the charge density with respect to the atoms and the elongation or contraction of the bonds after applying strain. When the distance between the atoms changes, the interaction between their charge densities is also modified, causing an energy shift of the valence and conduction bands and an increase or decrease of the E_{gap} [50].

Regarding the electronic transmission τ_{el} of the GB systems [Figs. 3(b) and 3(c)], there are clear differences between τ_{el} for pristine phosphorene (zigzag for GB1 and armchair for GB2) and the one corresponding to GB systems without and with strain. We first remark that the absence of midgap states in the transmission means that there are not unsaturated bonds in the strained systems, i.e., even at high strain values there are no broken bonds in the system. The inclusion of the 5|7 linear defect to form the GB1 system produces, as expected, a suppression of the electronic transmission channels in the plotted range of the spectrum of pristine ZZ phosphorene; see Fig. 3(b). This is originated from the scattering around the 5|7 defects and it comes together with a slight increment of E_{gap} [51]. In more detail, a combination of symmetry changes, bond-length alteration, and charge accumulation around the GB work together to modify the electronic transmission in the system. After applying uniaxial strain on the GB1 system, one can see that the transmission probability of the energies closer to the Fermi level E_{F} is slightly modified for low strain levels ($s < 4.0\%$). However, for larger strain levels, the valence and conduction bands are shifted towards E_F, reducing E_{gap}. Indeed, the GB1 system with $s = 10.48\%$ would be more favorable for doping-based electronic applications compared to its pristine counterpart due to the proximity of the conduction band to E_{F}. τ_{el} of pristine AC phosphorene experiences

a stronger suppression of the electronic transmission channels in both valence and conduction bands when 4|8 defects are considered; see Fig. 3(c). In particular, the valence band is the most affected, leading to an increase of E_{gap} from 1.8 to 3.0 eV. Similar to the GB1 system, small strain levels only slightly modified the transmission probability for energies at the band edges, while for $s > 10\%$ the transmission probability increases again and the valence-band edge is largely shifted towards E_F. There is also an increment in the transmission probability for the energy levels at the conduction-band edge, but for levels farther than these the probability reduces with the applied strain.

In brief, 5|7 (GB1) and 4|8 (GB2) defects degraded the electronic properties of their corresponding pristine counterpart, showing a more remarkable effect in the GB2 system where phosphorene increases its electronic band gap $\sim 50\%$ at zero strain. The influence of uniaxial strain on τ_{el} is very similar for both systems at $s < 4.0\%$, while for larger s, the behavior of the transmission probability of energy levels in the valence and conduction bands depends on the GB topology.

C. Thermal properties

Based on the influence of strain on the in-plane (IP) and out-of-plane (OP) bond lengths discussed above, we may expect changes in the thermal transport properties of both GB systems. Figure 4 displays the phonon transmission τ_{ph} and the corresponding thermal conductance κ_{ph} for GB1 and GB2 at different applied strains. For comparison, we also show these properties corresponding to pristine phosphorene along zigzag (ZZ) and armchair (AC) directions. As expected, the scattering originated by the 5|7 defects significantly decreases the overall τ_{ph} of pristine ZZ phosphorene [black line in Fig. 4(a)], the effect being more pronounced at higher frequencies ($\omega > 250\ \mathrm{cm}^{-1}$, optical branches) [52]. The transmission probability in this frequency range is also the most affected once a strain is applied. Indeed, even new transmission resonances emerge around $300\ \mathrm{cm}^{-1}$, closing the phonon gap found in both the strainless GB and the pristine ZZ phosphorene system. A calculation of the projected phonon density of states (PDOS) has revealed that these resonances are mainly produced by the strain-induced vibrational modes of atoms in the phosphorene regions excluding the GB atoms (see Fig. 7 in Appendix A). This is evidence of the usefulness of strain for phonon band-gap engineering in grain boundaries [53]. Moreover, we have found that the long-wavelength modes of the GB1 system ($\omega < 40\ \mathrm{cm}^{-1}$) are slightly affected at small strain levels ($s < 5.0\%$), but their transmission is then constantly reduced for larger s values. Similarly, 4|8 defects considerably suppress the overall τ_{ph} of pristine AC phosphorene [black line in Fig. 4(c)], having now a larger impact on vibrational modes with $\omega > 80\ \mathrm{cm}^{-1}$. Unlike the GB1 system, the effect of strain on τ_{ph} of the GB2 system is not uniform in the whole frequency spectrum. However, there is a constant shift of the optical modes towards lower frequencies, which leads to a reduction of the phonon gap around $300\ \mathrm{cm}^{-1}$, which is nevertheless not closed as for GB1. Interestingly, these strain-induced phonon shifts have also been observed in materials based on molybdenum disulfide and tungsten disulfide [54].

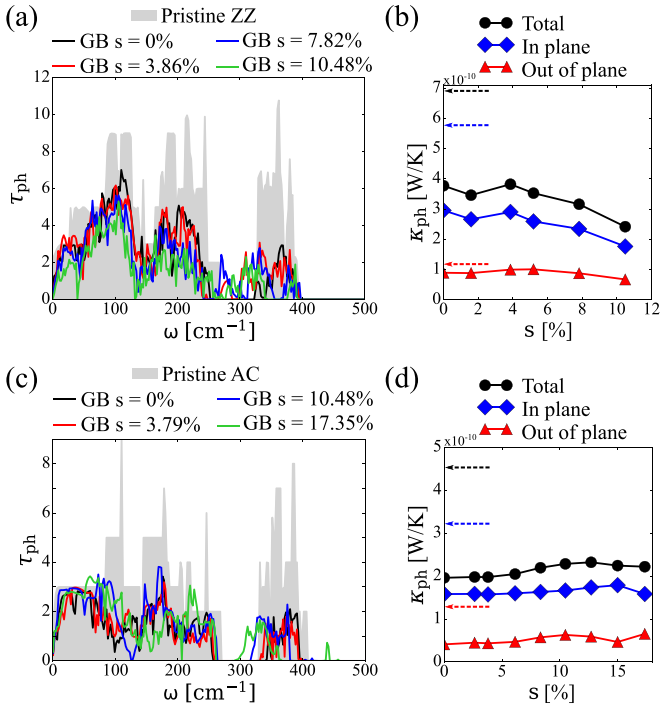

FIG. 4. Phonon transmission τ_{ph} as a function of the frequency ω of (a) GB1 and (c) GB2 systems without and with applied strain. As a reference, τ_{ph} of pristine phosphorene in the ZZ and AC directions was also included as a gray background. Thermal conductance κ_{ph} as a function of the strain for (b) GB1 and (d) GB2 systems. The black line corresponds to the total κ_{ph}, while the blue and red lines correspond to the IP and OP conductance, respectively. The dashed arrows represent the total (black), IP (blue), and OP (red) κ_{ph} of pristine phosphorene.

To have a better understanding of the thermal transport properties of the GB systems, the total κ_{ph} was also projected into their IP and OP contributions [see Figs. 4(b) and 4(d)]. κ_{ph} of pristine ZZ phosphorene is reduced [black arrow in Fig. 4(b)] by 40% down to 3.8×10^{-10} W/K after including the 5|7 defects to form the GB1 system. Moreover, κ_{ph} of the GB1 system remains almost unaltered for small strain levels, but for $s > 4\%$, κ_{ph} decreases, which is in agreement with the strain dependence of the corresponding τ_{ph}. Notice that the small increment of κ_{ph} at $s = 3.86\%$ may be correlated with the increase of transmission probability in the low-frequency range ($\omega < 50\ \mathrm{cm}^{-1}$). Analyzing the results in terms of IP (blue line) and OP (red line) contributions to total κ_{ph}, one can see that the IP modes dominate the thermal transport properties of both pristine and GB1 systems. Here, the 5|7 defects decreased the IP-κ_{ph} of the pristine counterpart by almost 50%, while the OP-κ_{ph} is only slightly reduced (10%). We have found that IP-κ_{ph} of the GB1 system is largely affected under the influence of uniaxial strain compared to OP-κ_{ph}, which agrees with our analysis of IP and OP bond lengths (see Fig. 2). κ_{ph} of the GB2 system shows, however, a different trend from the one previously discussed for GB1; see Fig. 4(d). First, the inclusion of 4|8 defects decreases the total κ_{ph} more than 50% compared with the pristine case. Secondly, κ_{ph} of the GB2 system remains almost constant independently of the applied strain, with some small

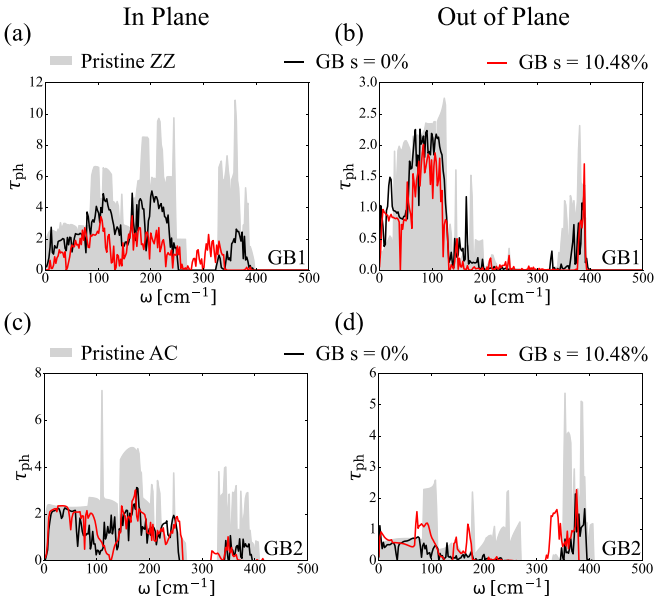

FIG. 5. (a),(c) In-plane (IP) and (b),(d) out-of-plane (OP) contributions to the total phonon transmission τ_{ph} as a function of the frequency ω for GB1 and GB2 systems without and with applied strain. As a reference, the IP and OP contributions to the total τ_{ph} for pristine phosphorene in the ZZ and AC directions were also included as a gray background.

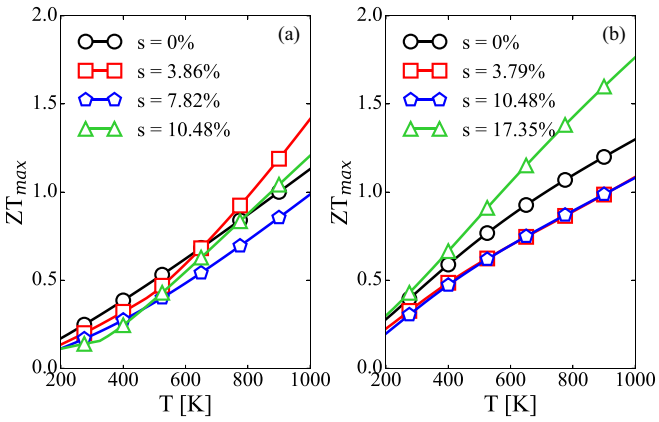

FIG. 6. Temperature dependence of the maximum value of the figure of merit (ZT_{max}) of (a) GB1 and (b) GB2 at different values of strain. The ZT_{max} considered for this plot is the maximum value obtained at each temperature in the optimal chemical potential (μ) value.

fluctuations after $s = 5\%$. The nearly constant behavior of κ_{ph} in GB2 can be explained by analyzing the τ_{ph} at different values of strain [see Fig. 4(c)], where some minimal changes can be noticed in the plotted spectrum, especially compared with GB1 [see Fig. 4(a)], which has a more notable decreasing trend. Finally, concerning the IP and OP contributions to κ_{ph}, they are reduced to 50% and 65% of the values corresponding to the pristine case after the formation of 4|8 defects. Also, similar to the total κ_{ph}, both contributions only slightly change up to $s = 15\%$, but at very high strain level, IP-κ_{ph} decreases and OP-κ_{ph} increases, leading to a certain degree of compensation, so that the total κ_{ph} is only weakly altered.

The strain dependence of IP- and OP-κ_{ph} can be rationalized by their corresponding τ_{ph}; see Fig. 5. For comparison, these quantities for pristine phosphorene along zigzag and armchair directions were also computed. Besides having larger transmission probability, it was found that IP-modes cover almost the whole frequency spectrum, while OP-modes are mostly located at low and very high frequencies for both GB systems. This verifies the predominance of IP modes in the thermal transport properties of the studied systems. As expected from our discussion of κ_{ph}, IP-τ_{ph} is reduced and OP-τ_{ph} is almost unaltered at a high strain level for the GB1 system [see Figs. 5(a) and 5(b)]. Moreover, the transmission peaks emerging in the phonon gap (around 300 cm^{-1}) correspond to IP-modes. Moving to the GB2 system, the inclusion of 4|8 defects significantly reduced OP-τ_{ph} of pristine AC phosphorene around 250 cm^{-1}, increasing the phonon gap from 40 to 100 cm^{-1}. Their IP- and OP-τ_{ph} do not present strong modifications up to $s = 10.48\%$ [see Figs. 5(c) and 5(d)], which is in agreement with the behavior of their associated κ_{ph}. At this strain, the transmission probability of both types of modes also increases around 100 cm^{-1} and the phonon gap is reduced, which causes a small increment of κ_{ph}, see Fig. 4(c).

D. Thermoelectric efficiency

After discussing the electronic and phonon transport properties of the GB systems, we proceed with the discussion of their thermoelectric performance. The main descriptor herewith is the figure of merit ZT, which is a dimensionless parameter defined as $ZT = \sigma S^2 T/\kappa$ [55]. ZT involves three basic quantities determining the efficiency of the energy conversion process: the electrical conductance σ, the Seebeck coefficient S, and the thermal conductance κ, the latter summing up both the electronic (κ_{el}) and phononic (κ_{ph}) components. The expressions to compute these transport quantities based on the quantum-mechanical electronic and phononic transmission functions are presented in Appendix B.

The maximum attainable value of the ZT (ZT_{max}) was calculated for both GB systems at different strain values, and it is displayed in Figs. 6(a) and 6(b) as a function of temperature. At room temperature and in the absence of any applied strain, the optimal thermoelectric performance is 0.28 and 0.43 for GB1 and GB2, respectively. Interestingly, both GBs show larger ZT than pristine phosphorene, which was reported to have $ZT \sim 0.2$ at room temperature [56]. As the temperature increases and for zero strain, ZT monotonously increases in a quasilinear fashion, with GB2 showing in general a larger ZT. This behavior is most likely related to the fact that GB2 has a considerably lower τ_{ph}. As can be seen in Figs. 4(a) and 4(c), in the frequency range around ~ 100 cm^{-1}, τ_{ph} in GB1 is almost 3× larger than in GB2. Therefore, although the PF is larger for GB1 due to the larger electronic conductance (see Appendix B), the final thermoelectric performance is reduced due to the larger impact of the heat conductance denominator.

Upon applying a strain in GB1, ZT decreases in proportion to the strain at room temperature, from 0.28 without strain to 0.15 when $s = 10.48\%$. This behavior is a result of the following two combined effects, namely the increase of κ_{el}

with increasing strain around the optimal μ, and the decrease of the Seebeck coefficient S with the applied strain. On the other hand, the strained GB2 system displays a different trend when the strain increases. For $s = 3.79\%$ and 10.48%, ZT has nearly identical values over the whole temperature range, although it takes lower values when compared to the strainless system. For an applied $s = 17.35\%$, on the contrary, GB2 outperforms all other cases.

IV. CONCLUSIONS

In summary, we have computed the electronic and thermal transport properties of two types of phosphorene grain boundaries, containing 5|7 and 4|8 defects, under applied strain along the transport direction. This was done combining a density-functional-based tight-binding approach with the atomistic Green's function method. Our bond analysis showed that in-plane bonds of GB1 have a higher stretch ratio with the applied strain compared with the out-of-plane bonds. The opposite effect is seen in the GB2 system, which also shows an irregular behavior due to the orientation of the phosphorene layers. The formation of grain boundaries into the phosphorene increases the band gap for both systems. However, the gap tends to decrease under the applied strain. Regarding the phonon transmission, 5|7 defects (GB1 system) considerably decrease the total transmission in the whole phonon spectrum, which then causes a decrease in the thermal conductance that is further reduced with the applied strain. In the GB2 system, the decrease of the phonon transmission was seen mostly above 100 cm^{-1} and also caused a decrease in the thermal conductance, but, in contrast with GB1, the applied strain led to a slight increase in the transmission. Although the electronic transmission and the corresponding power factor of GB1 are larger than for GB2, the larger thermal conductance of GB1 leads to overall smaller values of the figure of merit than for GB2. Regardless of that, both GB systems have a better thermoelectric performance than pristine phosphorene.

Our results are of interest for the further design of phosphorene GB systems towards thermoelectric devices, since we have shown that such structural defects have a different influence on the electronic and phononic transmission function, and thus on the corresponding linear conductances.

ACKNOWLEDGMENTS

This investigation has been supported through the German Research Foundation within the project "Straintronics of imperfect quasi-two-dimensional materials: coplanar vs lamellar hetero-structures" (Grant No. CU 44/43). We thank T. Radchenko, V. Tatarenko, and I. Sahalianov for useful discussions. We acknowledge the Center for Information Services and High Performance Computing (ZIH) at TU Dresden for providing the computational resources.

APPENDIX A: PROJECTED PHONON DENSITY OF STATES IN GB1

The projected phonon density of states (PDOS) has been calculated by using the Green's function formalism as follows [43]:

$$\mathrm{PDOS}(\omega) = \frac{i(G^r - G^a)\omega}{\pi B_{\mathrm{Fx}}}, \tag{A1}$$

where $G^{r/a}$ is the retarded/advanced Green's function of the device region with bond length B_{Fx}. We have focused this analysis on the frequency range $\omega \in [260 - 320]\ \mathrm{cm}^{-1}$ of τ_{ph} for the GB1 system to gain insights into the origin of the new transmission resonances that appear after applying uniaxial strain (see Fig. 7).

Figures 7(a)–7(c) show the real-space PDOS of the GB1 system under three different cases of strain: $s = 0\%$, 3.86%, and 7.82%. The color code is the level of contribution to the vibrational modes in the region selected for the analysis, i.e., dark blue and red correspond to the atoms with lowest and highest contribution, respectively. The values of the PDOS are normalized to the highest value between the three devices at different strain levels. We also plot the associated frequency-space PDOS at different strain levels; see Figs. 7(d)–7(f). The result in Fig. 7(a) shows that all atoms in the device region of the unstrained GB1 system are not contributing to vibrational modes with $\omega \in [260 - 320]\ \mathrm{cm}^{-1}$, which is clearly reflected on its frequency-space PDOS with the presence of a phonon band gap [see Fig. 7(d)].

After applying strain to the system, the phonon band gap is reduced due to new vibrational modes mainly originated by the atoms in the surroundings of the GB region [see Figs. 7(b) and 7(e)]. The phonon band gap disappears when the strain is above 7.8% [see Fig. 7(f)]. Here, the lowest contribution to the PDOS in this frequency region comes from the GB atoms, while the rest of the atoms of the device region are the main contributors to the emergence of the vibrational modes that fill the phonon band gap. Thus, vibrations associated with GB atoms at these frequencies are less susceptible to structural changes produced by the applied uniaxial strain compared to the other atoms.

APPENDIX B: THERMOELECTRIC TRANSPORT PROPERTIES

Within the framework of nonequilibrium thermodynamics together with the Landauer approach for transport, the thermoelectric transport properties of the GB systems were computed. All the scattering processes considered are elastic and mediated by structural features of the system, meaning that the phonon-phonon interaction is not considered through this approach. Additionally, electron-phonon coupling is not addressed, so we can deal separately with electronic and phononic transport channels. Upon expansion of the electrical current under small applied voltage and temperature biases, the electronic transport coefficients that conform the figure of merit ZT can be calculated as

$$\sigma = e^2 \Lambda_0, \tag{B1}$$

$$S = \frac{1}{qT}\frac{\Lambda_1}{\Lambda_0}, \tag{B2}$$

$$\kappa_{\mathrm{el}} = \frac{1}{T}\left[\Lambda_2 - \frac{\Lambda_1^2}{\Lambda_0}\right], \tag{B3}$$

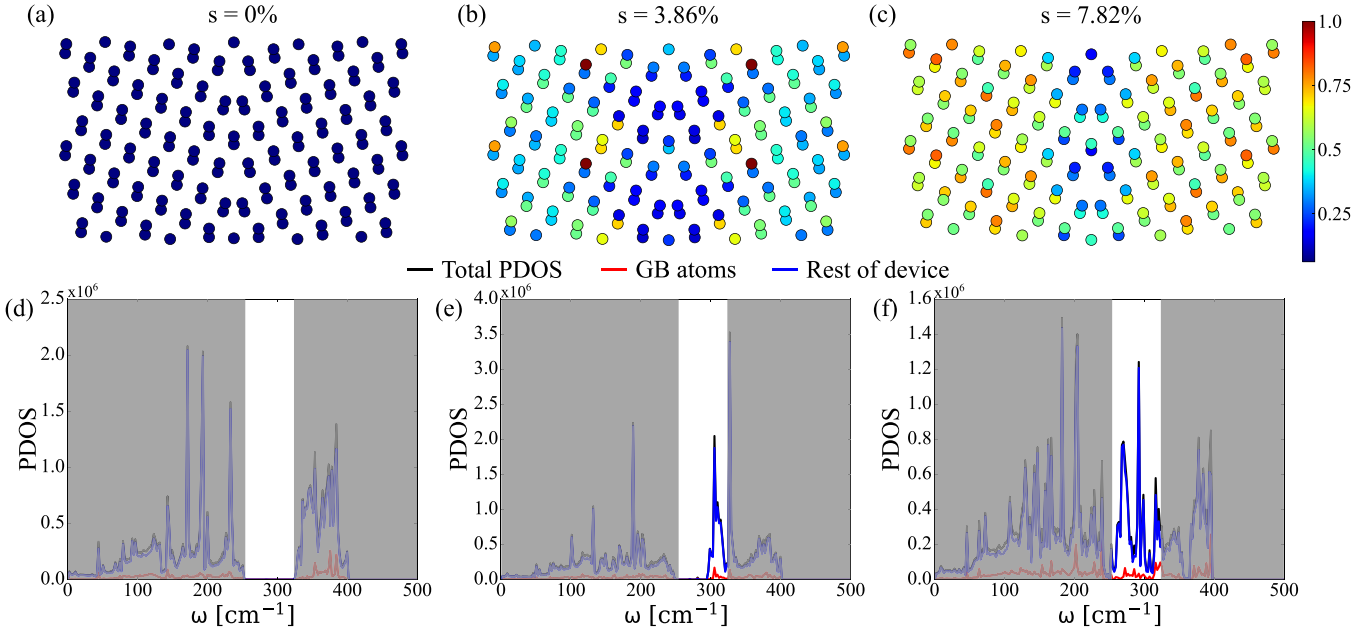

FIG. 7. Real-space projection of the phonon density of states (PDOS) of the device region in the GB1 system with (a) 0%, (b) 3.86%, and (c) 7.82% applied strain. The values of PDOS are normalized to the highest value between the three devices, and the colorbar (right side) scales the contribution of each atom, where dark blue indicates zero contribution, and red is the highest contribution. The PDOSs as a function of the frequency corresponding to the systems analyzed in panels (a)–(c) are plotted in panels (d)–(f). We show the total PDOS (black) together with the contribution from the atoms in the grain boundary (red) and in the rest of the device (blue). We have added the blocks in gray to highlight the frequency range for this analysis, 260–320 cm^{-1}.

where q is the electric charge of carriers, positive for holes and negative for electrons, and the moments Λ_m involve the electronic transmission function $\tau_{\rm el}$ as

$$\Lambda_m = \frac{2}{h}\int dE(E-\mu)^m\Big[-\frac{\delta f(E,\mu,T)}{\delta E}\Big]\tau_{\rm el}(E), \qquad \text{(B4)}$$

with $f(E,\mu,T)$ being the Fermi-Dirac distribution function, μ the chemical potential, and h the Planck constant. The μ is used as an independent variable to address the influence of doping on the system, since it can be associated with the carrier concentration.

In Fig. 8, we show the electronic contribution to the thermal conductance $\kappa_{\rm el}$, the Seebeck coefficient S, and the power factor (PF $= \sigma S^2$) of the GB1 with different values of strain as a function of the chemical potential μ at 300 and 600 K. As a matter of clarity, positive μ corresponds to n-type doping and negative μ to p-type doping. Figures 8(a) and 8(b) display $\kappa_{\rm el}$ as a function of μ, which has a similar profile to the previously discussed $\tau_{\rm el}$ from Fig. 3(b). When temperature raises, the overall $\kappa_{\rm el}$ increases for all the systems due to the large broadening of the Fermi function derivative under the integrals of the Λ_m moments in Eq. (B4). With regard to S, displayed in Figs. 8(c) and 8(d), the GB1 with $s = 0\%$ shows a symmetric profile with the highest value compared with the strained systems. On the other hand, the other systems decrease their S in proportion to the strain, and also the symmetry of the profile is lost, showing that p-type systems would perform better at 300 K. But the S profile for these systems changes when the temperature increases, as can be seen in the plot at 600 K, where the systems recover their symmetry and increase more their performance in comparison to the strain-

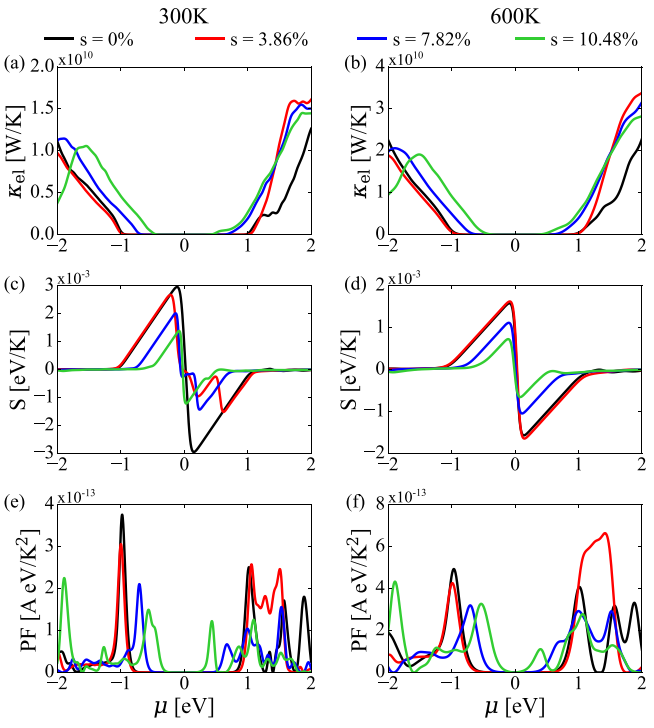

FIG. 8. Thermoelectric transport properties of GB1 at 300 K (left side) and 600 K (right side) at different values of strain. We show the variation in the (a),(b) electronic contribution to the thermal conductance ($\kappa_{\rm el}$), (c),(d) the Seebeck coefficient (S), and (e),(f) the power factor (PF) as a function of the chemical potential μ.

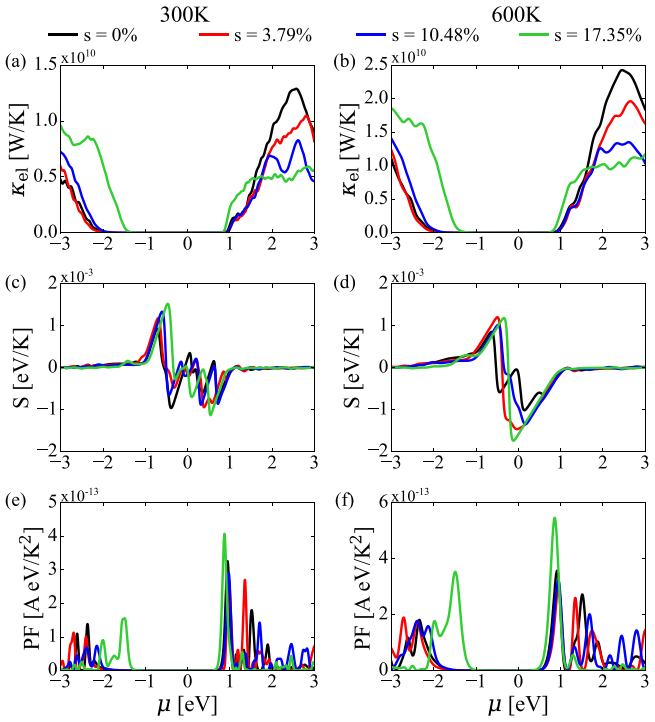

FIG. 9. Thermoelectric transport properties of GB2 at 300 K (left side) and 600 K (right side) at different values of strain. We show the variation in the (a),(b) electronic contribution to the thermal conductance (κ_{el}), (c),(d) the Seebeck coefficient (S), and (e),(f) the power factor (PF) as a function of the chemical potential μ.

less system, especially the system with $s = 3.86\%$, which has the same value of S as the GB1 without strain. Finally, the PF is presented in Figs. 8(e) and 8(f), where the strainless system remains as the best choice at room temperature, having the largest peak at $\mu = -1$ eV. The PF for the other systems decreases in proportion to the strain, but the highest peak is displaced along the μ toward 0 eV, which makes it convenient for practical purposes, where the system does not require such a high carrier concentration. At higher temperature, the *PF* increases in all the systems, but $s = 3.86\%$ displays a large increase in the *n*-type doping region, overcoming the performance of the strainless system. This result is correlated with the large difference in τ_{el} between these systems at around 1.5 eV (see Fig. 3).

Similar thermoelectric analysis was carried out for the GB2 system, presented in Fig. 9, for the same thermoelectric parameters and temperatures. In contrast with GB1, the results of κ_{el} [see Figs. 9(a) and 9(b)] are shown to be considerably smaller in the negative side of the μ, except when the strain value is pretty high ($s = 17.35\%$), which then reaches similar values to those of the other systems in GB1. But on the positive side of μ the trend is different, i.e., the strainless system has the largest value and then it decreases as a function of the applied strain. It is also important to mention that the regions with larger κ_{el} are farther from the neutral carrier concentration point ($\mu = 0$) than was seen in the GB1 systems. This is a consequence of the opening of the band gap in the GB2 system. When the temperature increases, so does κ_{el}, but in smaller proportion. This was seen for GB1 systems, which can potentially be in favor of the employment of the GB2 systems as thermoelectric systems at higher temperatures, since the not-so-large values of κ_{el} will then not decrease so much the ZT. Regarding the S [see Figs. 9(c) and 9(d)], and in contrast to the GB1 system, all the GB2 systems do not have an symmetric profile at low or higher temperature. The system with $s = 17.35\%$ shows the highest peaks on both sides with values above $|1$ eV/K$|$. At 600 K, the S increases for all the systems, and the largest values are shifted toward the neutral carrier concentration point, which again favors their potential usage for thermoelectric devices. Finally, the PF for these systems [see Figs. 9(e) and 9(f)] is very low on the negative side of μ, meaning that *p*-type carriers do not benefit this system for thermoelectric devices. On the other hand, the positive side of the plot shows good results for the GB2 systems, especially for the GB2 system with $s = 17.37\%$, which reaches 4.1 A eV/K^2 at 0.95 eV. Similar results are obtained at 600 K, where an increase in the PF for all the systems is notable. The decrease of κ_{el} and the increase of PF as a function of the strain may make it possible for strained GB2 devices to be employed for thermoelectric devices.

[1] K. S. Novoselov, A. K. Geim, S. V. Morozov, D. Jiang, Y. Zhang, S. V. Dubonos, I. V. Grigorieva, and A. A. Firsov, Electric field effect in atomically thin carbon films, Science **306**, 666 (2004).

[2] N. Briggs, S. Subramanian, Z. Lin, X. Li, X. Zhang, K. Zhang, K. Xiao, D. Geohegan, R. Wallace, L.-Q. Chen, M. Terrones, A. Ebrahimi, S. Das, J. Redwing, C. Hinkle, K. Momeni, A. van Duin, V. Crespi, S. Kar, and J. A. Robinson, A roadmap for electronic grade 2D materials, 2D Mater. **6**, 022001 (2019).

[3] Z. Xiong, L. Zhong, H. Wang, and X. Li, Structural defects, mechanical behaviors and properties of two-dimensional materials, Materials **14**, 1192 (2021).

[4] P. Ares and K. S. Novoselov, Recent advances in graphene and other 2d materials, NMS **4**, 3 (2022), special issue on Graphene and 2D Alternative Materials.

[5] M. Xu, T. Liang, M. Shi, and H. Chen, Graphene-like two-dimensional materials, Chem. Rev. **113**, 3766 (2013).

[6] R. Mas-Ballesté, C. Gómez-Navarro, J. Gómez-Herrero, and F. Zamora, 2d Materials: To graphene and beyond, Nanoscale **3**, 20 (2011).

[7] M. Galluzzi, Y. Zhang, and X.-F. Yu, Mechanical properties and applications of 2D black phosphorus, J. Appl. Phys. **128**, 230903 (2020).

[8] B. Li, C. Lai, G. Zeng, D. Huang, L. Qin, M. Zhang, M. Cheng, X. Liu, H. Yi, C. Zhou, F. Huang, S. Liu, and Y. Fu, Black phosphorus, a rising star 2D nanomaterial in the post-graphene era: Synthesis, properties, modifications, and photocatalysis applications, Small **15**, 1804565 (2019).

[9] J. R. Brent, N. Savjani, E. A. Lewis, S. J. Haigh, D. J. Lewis, and P. O'Brien, Production of few-layer phosphorene by liquid

exfoliation of black phosphorus, Chem. Commun. **50**, 13338 (2014).
[10] M. Akhtar, G. Anderson, R. Zhao, A. Alruqi, J. E. Mroczkowska, G. Sumanasekera, and J. B. Jasinski, Recent advances in synthesis, properties, and applications of phosphorene, npj 2D Mater. Appl. **1**, 5 (2017).
[11] L. Liang, J. Wang, W. Lin, B. G. Sumpter, V. Meunier, and M. Pan, Electronic bandgap and edge reconstruction in phosphorene materials, Nano Lett. **14**, 6400 (2014).
[12] C. Guo, T. Wang, C. Xia, and Y. Liu, Modulation of electronic transport properties in armchair phosphorene nanoribbons by doping and edge passivation, Sci. Rep. **7**, 12799 (2017).
[13] Y. Cai, G. Zhang, and Y. W. Zhang, Layer-dependent band alignment and work function of few-layer phosphorene, Sci. Rep. **4**, 6677 (2015).
[14] J. M. G. Hernandez, J. G. Sanchez, H. N. F. Escamilla, G. H. Cocoletzi, and N. Takeuchi, First-principles studies of the strain-induced band-gap tuning in black phosphorene, J. Phys.: Condens. Matter **33**, 175502 (2021).
[15] V. Sorkin and Y. W. Zhang, Mechanical properties and failure behavior of phosphorene with grain boundaries, Nanotechnology **28**, 075704 (2017).
[16] G. S. Rohrer, Grain boundary energy anisotropy: A review, J. Mater. Sci. **46**, 5881 (2011).
[17] L. Zhang, C. Lu, and K. Tieu, A review on atomistic simulation of grain boundary behaviors in face-centered cubic metals, Comput. Mater. Sci. **118**, 180 (2016).
[18] H. Vahidi, K. Syed, H. Guo, X. Wang, J. L. Wardini, J. Martinez, and W. J. Bowman, A review of grain boundary and heterointerface characterization in polycrystalline oxides by (scanning) transmission electron microscopy, Crystals **11**, 878 (2021).
[19] F. Gargiulo, Electronic transport across realistic grain boundaries in graphene, arXiv:2107.06784.
[20] M. Khalkhali, A. Rajabpour, and F. Khoeini, Thermal transport across grain boundaries in polycrystalline silicene: A multiscale modeling, Sci. Rep. **9**, 5684 (2019).
[21] J. Sun, J. Leng, and G. Zhang, The grain boundary effect on mechanical and electronic transport properties of a striped borophene, Phys. Chem. Chem. Phys. **22**, 21844 (2020).
[22] Y. Guo, S. Zhou, J. Zhang, Y. Bai, and J. Zhao, Atomic structures and electronic properties of phosphorene grain boundaries, 2D Mater. **3**, 025008 (2016).
[23] Z.-L. Zhu, W.-Y. Yu, X.-Y. Ren, Q. Sun, and Y. Jia, Grain boundary in phosphorene and its unique roles on C and O doping, Europhys. Lett. **109**, 47003 (2015).
[24] Y. Liu, F. Xu, Z. Zhang, E. S. Penev, and B. I. Yakobson, Two-dimensional mono-elemental semiconductor with electronically inactive defects: The case of phosphorus, Nano Lett. **14**, 6782 (2014).
[25] Y. Guo, C. Qiao, A. Wang, J. Zhang, S. Wang, W.-S. Su, and Y. Jia, The fracture behaviors of monolayer phosphorene with grain boundaries under tension: A molecular dynamics study, Phys. Chem. Chem. Phys. **18**, 20562 (2016).
[26] X. Wang, Q. Wang, X. Liu, Z. Huang, and X. Liu, Phosphorene grain boundary effect on phonon transport and phononic applications, Nanotechnology **33**, 265704 (2022).
[27] X. Liu, J. Gao, G. Zhang, J. Zhao, and Y. W. Zhang, Remarkable role of grain boundaries in the thermal transport properties of phosphorene, ACS Omega **5**, 17416 (2020).
[28] Z. Dai, L. Liu, and Z. Zhang, Strain engineering of 2d materials: Issues and opportunities at the interface, Adv. Mater. **31**, 1805417 (2019).
[29] Z. Peng, X. Chen, Y. Fan, D. J. Srolovitz, and D. Lei, Strain engineering of 2D semiconductors and graphene: from strain fields to band-structure tuning and photonic applications, Light Sci. Appl. **9**, 190 (2020).
[30] S. Yang, Y. Chen, and C. Jiang, Strain engineering of two-dimensional materials: Methods, properties, and applications, InfoMat **3**, 397 (2021).
[31] M. Raeisi, S. Ahmadi, and A. Rajabpour, Modulated thermal conductivity of 2D hexagonal boron arsenide: A strain engineering study, Nanoscale **11**, 21799 (2019).
[32] K. Nakagawa, K. Satoh, S. Murakami, K. Takei, S. Akita, and T. Arie, Controlling the thermal conductivity of multilayer graphene by strain, Sci. Rep. **11**, 19533 (2021).
[33] L. M. Sandonas, R. Gutierrez, A. Pecchia, G. Seifert, and G. Cuniberti, Tuning quantum electron and phonon transport in two-dimensional materials by strain engineering: A green's function based study, Phys. Chem. Chem. Phys. **19**, 1487 (2017).
[34] S. B. Kumar and J. Guo, Strain-induced conductance modulation in graphene grain boundary, Nano Lett. **12**, 1362 (2012).
[35] Y. Liu, X. Zou, and B. I. Yakobson, Dislocations and grain boundaries in two-dimensional boron nitride, ACS Nano **6**, 7053 (2012).
[36] W. Zhou, X. Zou, S. Najmaei, Z. Liu, Y. Shi, J. Kong, J. Lou, P. M. Ajayan, B. I. Yakobson, and J. C. Idrobo, Intrinsic structural defects in monolayer molybdenum disulfide, Nano Lett. **13**, 2615 (2013).
[37] B. Aradi, B. Hourahine, and T. Frauenheim, Dftb+, a sparse matrix-based implementation of the DFTB method, J. Phys. Chem. A **111**, 5678 (2007).
[38] Álvaro Rodríguez Méndez, L. M. Sandonas, A. Dianat, R. Gutierrez, and G. Cuniberti, An atomistic study of the thermoelectric signatures of cnt peapods, J. Phys. Chem. C **125**, 13721 (2021).
[39] C. He, G. Liu, W. X. Zhang, Z. Q. Shi, and S. L. Zhou, Tuning the structures and electron transport properties of ultrathin cu nanowires by size and bending stress using DFT and DFTB methods, RSC Adv. **5**, 22463 (2015).
[40] A. Pecchia, L. Latessa, A. Di Carlo, P. Lugli, and T. Neihaus, Electronic transport properties of molecular devices, Phys. E **19**, 139 (2003), fourth International Symposium on Nanostructures and Mesoscopic Systems.
[41] M. Gaus, Q. Cui, and M. Elstner, DFTB3: Extension of the self-consistent-charge density-functional tight-binding method (scc-dftb), J. Chem. Theory Comput. **7**, 931 (2011).
[42] H. Sevinçli, S. Roche, G. Cuniberti, M. Brandbyge, R. Gutierrez, and L. M. Sandonas, Green function, quasi-classical Langevin and Kubo–Greenwood methods in quantum thermal transport, J. Phys.: Condens. Matter **31**, 273003 (2019).
[43] W. Zhang, T. S. Fisher, and N. Mingo, The atomistic Green's function method: An efficient simulation approach for nanoscale phonon transport, Numer. Heat Transf., Pt. B **51**, 333 (2007).
[44] A. Pecchia, G. Penazzi, L. Salvucci, and A. D. Carlo, Non-equilibrium Green's functions in density functional tight binding: Method and applications, New J. Phys. **10**, 065022 (2008).

[45] L. Medrano Sandonas, R. Gutierrez, A. Pecchia, A. Croy, and G. Cuniberti, Quantum phonon transport in nanomaterials: Combining atomistic with non-equilibrium Green's function techniques, Entropy **21**, 735 (2019).

[46] O. V. Yazyev and S. G. Louie, Topological defects in graphene: Dislocations and grain boundaries, Phys. Rev. B **81**, 195420 (2010).

[47] T. Nakanishi, S. Yoshida, K. Murase, O. Takeuchi, T. Taniguchi, K. Watanabe, H. Shigekawa, Y. Kobayashi, Y. Miyata, H. Shinohara, and R. Kitaura, The atomic and electronic structure of 0° and 60° grain boundaries in MOS2, Front. Phys. **7**, 59 (2019).

[48] Y. Lu and J. Guo, Band gap of strained graphene nanoribbons, Nano Res. **3**, 189 (2010).

[49] N.-C. Ri, J.-C. Kim, and S.-I. Ri, Effect of strain on mechanical, electronic, and transport properties of hybrid armchair graphane/graphene/fluorographane nanoribbon, Chem. Phys. Lett. **765**, 138311 (2021).

[50] Y. Zhang, X. Wu, Q. Li, and J. Yang, Linear band-gap modulation of graphane nanoribbons under uniaxial elastic strain: A density functional theory study, J. Phys. Chem. C **116**, 9356 (2012).

[51] Q. G. Zhang, X. Zhang, B. Y. Cao, M. Fujii, K. Takahashi, and T. Ikuta, Influence of grain boundary scattering on the electrical properties of platinum nanofilms, Appl. Phys. Lett. **89**, 114102 (2006).

[52] M. Schrade, K. Berland, S. N. Eliassen, M. N. Guzik, C. Echevarria-Bonet, M. H. Sørby, P. Jenuš, B. C. Hauback, R. Tofan, A. E. Gunnæs, C. Persson, O. M. Løvvik, and T. G. Finstad, The role of grain boundary scattering in reducing the thermal conductivity of polycrystalline XNISN (x = hf, zr, ti) half-heusler alloys, Sci. Rep. **7**, 13760 (2017).

[53] J.-W. Jiang, Phonon bandgap engineering of strained monolayer MOS2, Nanoscale **6**, 8326 (2014).

[54] F. Wang, I. A. Kinloch, D. Wolverson, R. Tenne, A. Zak, E. O'Connell, U. Bangert, and R. J. Young, Strain-induced phonon shifts in tungsten disulfide nanoplatelets and nanotubes, 2D Mater. **4**, 015007 (2016).

[55] G. J. Snyder and A. H. Snyder, Figure of merit zt of a thermoelectric device defined from materials properties, Energy Environ. Sci. **10**, 2280 (2017).

[56] L. Medrano Sandonas, D. Teich, R. Gutierrez, T. Lorenz, A. Pecchia, G. Seifert, and G. Cuniberti, Anisotropic thermoelectric response in two-dimensional puckered structures, J. Phys. Chem. C **120**, 18841 (2016).